ACS APPLIED ENERGY MATERIALS

www.acsaem.org

Article

Engineering Hexagonal/Monoclinic WO_3 Phase Junctions for Improved Electrochemical Hydrogen Evolution Reaction

Giacometta Mineo, Mario Scuderi, Elena Bruno, and Salvo Mirabella*

Cite This: *ACS Appl. Energy Mater.* 2022, 5, 9702−9710

Read Online

ACCESS | Metrics & More | Article Recommendations | Supporting Information

ABSTRACT: Electrochemical hydrogen evolution reaction (HER) is one of the most promising green methods used to produce renewable and sustainable energy. The development of a highly efficient Pt-free electrocatalyst for HER is a crucial point for the ecosustainability and cost reduction of this method. Herein, WO_3 nanorods were synthesized by a hydrothermal method and calcinated in air at 400 °C for different times (30, 60, and 90 min). Experimental investigation involved SEM, TEM, XRD, and electrochemical analyses such as linear sweep voltammetry (LSV), cyclic voltammetry (CV), electrochemical impedance spectroscopy (EIS), and Mott Schottky analysis. Calcination at 400 °C induces a peculiar crystal phase transition driven by the formation of hexagonal/monoclinic WO_3 phase junctions. The best HER performance (170 mV overpotential for 10 mA/cm^2) is obtained when WO_3 nanorods show comparable volumes of hexagonal and monoclinic phases (after 60 min annealing). The effect of phase junction on HER catalysis sustained by WO_3 nanorods is investigated in detail, opening the route of efficient, Pt-free catalysts for HER application.

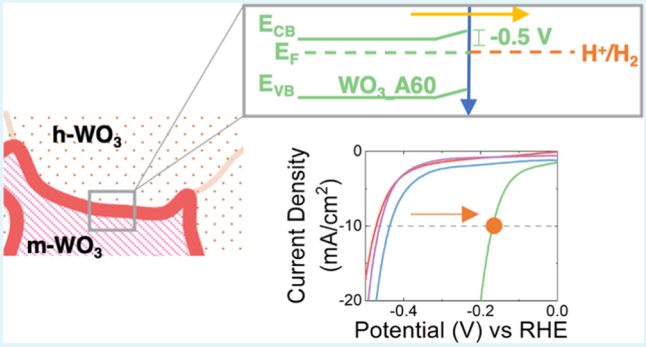

KEYWORDS: *hydrogen evolution reaction, WO_3, electrocatalyst, phase junction, band bending, Pt-free catalyst*

1. INTRODUCTION

The finite supply of fossil fuels, the climate change, and the growing world energy demand inspire the scientific community for developing renewable and sustainable energy sources, among which H_2 attracts a lot of awareness. One of the most promising green methods to produce highly pure H_2 on a large scale, with zero carbon emission, sustainability, recyclability, and ecofriendliness is water electrolysis through hydrogen and oxygen evolution reactions at the cathode and anode, respectively.[1−3] The most active catalysts for the hydrogen evolution reaction (HER) are Pt-based materials, but the large-scale application with these catalysts is limited by the low availability and high cost of Pt;[4,5] indeed, several earth-abundant transition metal-based electrocatalysts have been studied for HER, both in acidic and alkaline media, such as transition-metal oxides.[6−9] Among them, WO_3 has emerged as a favorable material thanks to its large availability and advantageous properties.[10−15]

Indeed, WO_3 is an *n*-type semiconductor with abundant reserves, high electrochemical stability in acidic environments, tunable band gap, and good proton conduction; unfortunately, as a semiconductor, it has poor electron transport ability and few active sites hindering high HER performances.[4,16,17] These negative aspects can be strongly reduced by an effective strategy using nanostructures, with high surface-to-volume ratio and low resistance to further improve the electrochemical properties, of WO_3 as cathodes for HER. WO_3 nanostructures can be effectively synthesized by hydrothermal,[18] sputtering,[19] thermal evaporation,[20] sol−gel,[21] and electrodeposition[22] methods. Nevertheless, in its pristine form, nanostructured WO_3 does not give excellent HER performances, as the atomic hydrogen adsorption free energy (ΔG_H) on the W site is high, leading to a poor HER activity, as explained by Sabatier's principle, for which ΔG_H close to zero gives better catalytic performances.[4,23,24] Many efforts have been made with the aim of modulating the WO_3 electronic structure, such as decoration with Pt clusters,[25,26] the embedding of W-based compounds on conductive supports such as reduced graphene oxide (RGO)[17] and carbon nanotubes (CNTs),[11] and the realization of heterostructures by coupling WO_3 with other transition-metal oxides.[27−29] Although these solutions are effective for enhancing the HER activity, their exploitation on a large scale is limited by the complex synthesis and assembly processes.

Received: May 5, 2022
Accepted: July 13, 2022
Published: July 22, 2022

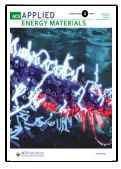

Downloaded via CNR on January 17, 2023 at 14:40:06 (UTC).
See https://pubs.acs.org/sharingguidelines for options on how to legitimately share published articles.

ACS Publications

© 2022 The Authors. Published by American Chemical Society

https://doi.org/10.1021/acsaem.2c01383
ACS Appl. Energy Mater. 2022, 5, 9702−9710

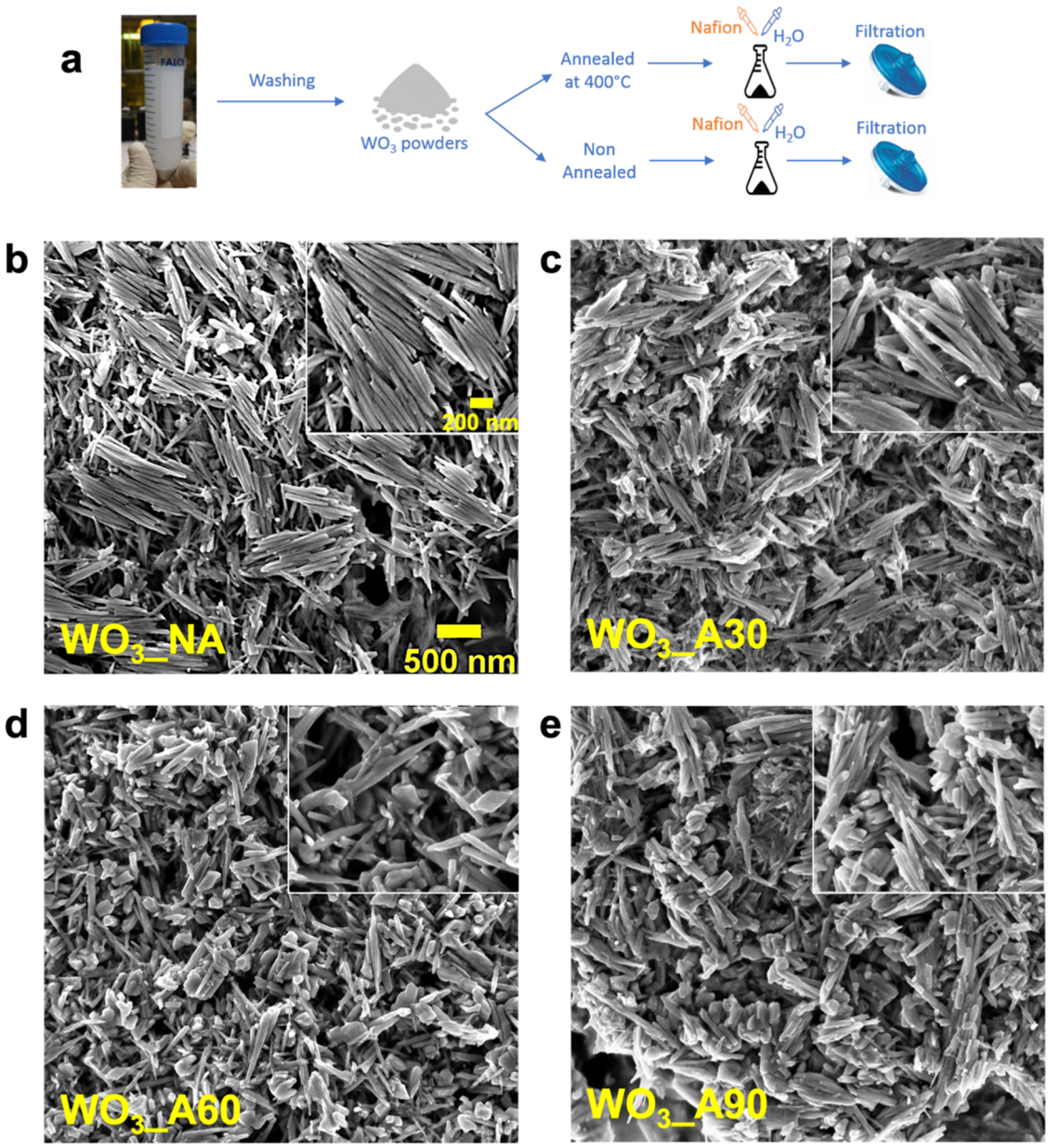

Figure 1. (a) WO_3 powder extraction, annealing, and filtering; low- and high- (inset) magnification SEM images of (b) WO_3_NA-, (c) WO_3_A30-, (d) WO_3_A60-, and (e) WO_3_A90-based electrodes. Markers in (a) are valid for all relative images.

The crystal phase of WO_3 can also play a pivotal role. The hexagonal structure of WO_3 seems to be the most performing for electrochemical applications due to the favorable H^+ intercalation−release pathways,[30] while the monoclinic phase is more stable at room temperature.[31] The mixed hexagonal−monoclinic WO_3-based heterostructure has been recently shown to enhance the photoelectrochemical ability by means of a Z-scheme in energy bands, promoting electron−hole pair separation.[32,33] Such a heterostructure can be extremely interesting for HER as the hexagonal−monoclinic interface can act as an active site for H^+ adsorption thanks to the formation of an electron reservoir promoting the catalytic and electrical properties.

Here, we report a low-cost and simple hydrothermal synthesis of a WO_3-based hexagonal−monoclinic phase junction heterostructure with excellent HER performances, evidenced by detailed structural and electrochemical characterization. A comprehensive description of the HER mechanism at the interface of the phase junction is also provided.

2. EXPERIMENTAL SECTION

2.1. Synthesis of WO_3 Nanorods. Hexagonal WO_3 nanorods are synthesized by using hydrothermal synthesis, as reported in our previous work.[34] WO_3 powder (Figure 1a) is obtained by centrifugation (6000 rpm for 10 min), followed by washing with ethanol and water several times, and finally drying on a hot plate for 1 h in air at 70 °C (denoted as WO_3_NA). Some samples underwent a calcination process on a hot plate at 400 °C for 30, 60, and 90 min (denoted as WO_3_A30, WO_3_A60, and WO_3_A90, respectively).

2.2. Preparation of Electrodes. The obtained WO_3-based nanostructures were used for the realization of different pastes (20 mg of nanostructure powder, 0.1 mL of Nafion, and 2 mL of deionized water, with subsequent filtration by a 1.2 μm filter), as shown in Figure 1a. Electrodes are produced by drop-casting the obtained WO_3-based pastes on graphene paper substrates (GP, 2 × 1 cm^2, Sigma Aldrich, 240 μm thick). The masses of the electrode

https://doi.org/10.1021/acsaem.2c01383
ACS Appl. Energy Mater. 2022, 5, 9702−9710

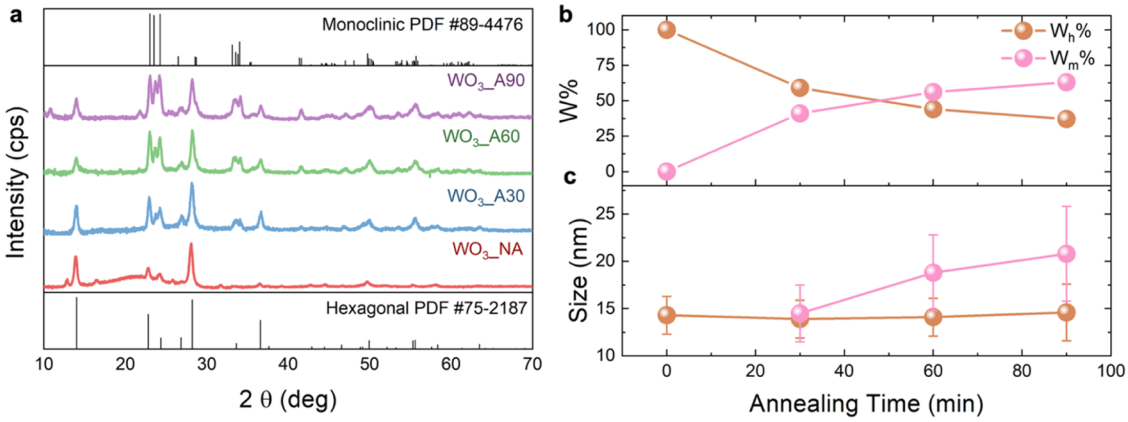

Figure 2. (a) XRD patterns of WO_3_NA, WO_3_A30, WO_3_A60, and WO_3_A90 powders, compared with pure hexagonal and monoclinic WO_3 XRD patterns; (b) weight ratio (W%) and (c) crystallite sizes of h-WO_3 and m-WO_3 (brown and pink spheres) as a function of annealing time for WO_3-based powders.

(substrate + WO_3 nanostructures) and the bare substrate were measured by a Mettler Toledo MX5 microbalance (sensitivity: 0.01 mg).

2.3. Characterization. The morphological analyses were carried out by a scanning electron microscope Gemini Field Emission SEM Carl Zeiss SUPRATM 25 (FEG-SEM, Carl Zeiss Microscopy GmbH, Jena, Germany) in lens mode and a transmission electron microscope (JEOL, JEM-ARM200F) operated in TEM mode. The film structure was analyzed through XRD using a SmartLab Rigaku diffractometer, at grazing incidence of 0.5°, equipped with a rotating anode of Cu Kα radiation operating at 45 kV and 200 mA. The scans were acquired from 10° to 70° with steps of 0.02°. The electrochemical measurements were performed at room temperature by using a potentiostat (VersaSTAT 4, Princeton Applied Research, USA) and a three-electrode setup, with a graphite rod electrode as the counter electrode (to avoid any Pt contaminations), a saturated calomel electrode (SCE) as the reference, and WO_3 onto GP as the working electrode, in 1 M H_2SO_4 supporting electrolyte.

2.4. Electrochemical Measurements. Electric current values were normalized to the geometrical immersed surface area of each electrode. The measured potential versus SCE was converted into the reversible hydrogen electrode (RHE) according to the Nernst equation:[28,35]

$$E'_{RHE} = E^{\Theta}_{SCE} + E_{SCE} \times 0.059 \times pH \quad (1)$$

where E^{Θ}_{SCE} is the standard potential of SCE at 25 °C (0.241 V), and E_{SCE} is the measured potential versus SCE. The HER activities of various WO_3-based electrodes were investigated using linear sweep voltammetry (LSV), recorded at 5 mV/s from −0.2 to −0.8 V versus SCE. Electrochemical impedance spectroscopy (EIS) was performed from 100 kHz to 0.1 Hz in a potentiostatic mode, with an AC voltage of 5 mV at the potential (vs SCE) of 10 mA/cm^2 in the LSV curves. The double-layer capacity (C_{dl}) was determined from the cyclic voltammetry (CV) curves, recorded at different scan rates (5 to 100 mV/s) from −0.2 to −0.3 V versus SCE. All the obtained potentials vs RHE are manually corrected by iR_u compensation as follows:

$$E_{RHE} = E'_{RHE} - iR_u \quad (2)$$

where i is the electrode current, and R_u [ohms] is the uncompensated resistance, measured by EIS.[1] The Mott−Schottky analyses were carried out from −0.2 to −1.6 V versus SCE at 1000 Hz frequency.

3. RESULTS AND DISCUSSION

3.1. Morphological Characterization. Figure 1b−e shows the low- and high- (inset) magnification SEM images of WO_3_NA-, WO_3_A30-, WO_3_A60-, and WO_3_A90-based electrodes, which appear composed of oddly aligned nanorods (0.5−1 μm long and 50 nm large; see inset in Figure 1) stacked on top of each other until they form a homogeneous and very porous film, which does not change by the thermal treatment, as also reported in the literature.[32]

A change in the phase structure of WO_3-based nanostructures during annealing processes was analyzed as a function of annealing time. Figure 2a shows the XRD patterns of WO_3_NA, WO_3_A30, WO_3_A60, and WO_3_A90 powders compared with the XRD patterns of hexagonal (PDF #89-4476) and monoclinic (PDF #75-2187) WO_3, respectively. The XRD pattern of WO_3_NA shows typical diffraction peaks related to the hexagonal crystal structure, which appear at 2θ = 14.00°, 24.36°, 26.84°, 28.22°, 33.62°, 36.58°, and 49.95° as expected, indicating the pure hexagonal phase in as-prepared WO_3 nanorods.[34] Besides the abovementioned diffraction peaks, with the increasing of annealing time, peaks clearly related to the monoclinic crystal structure appear (2θ = 23.00°, 23.50°, 24.28°, 33.12°, 33.54°, 33.84°, 34.04°, 49.74°, and 55.71°) with the increasing intensity, suggesting the coexistence of hexagonal and monoclinic WO_3 phases (h-WO_3 and m-WO_3) in WO_3_A30, WO_3_A60, and WO_3_A90 powders. Therefore, according to the XRD results shown in Figure 2a, h-WO_3 starts to change phase toward m-WO_3 as soon as the annealing process begins.

By using the RIR method, the weight ratio (W%) of h-WO_3 and m-WO_3 (W_h% and W_m%, respectively) in WO_3_NA, WO_3_A30, WO_3_A60, and WO_3_A90 powders can be calculated (details are reported in the Supporting Information), and Figure 2b shows the obtained values for W_h% and W_m% as a function of annealing time. The intensities of m-WO_3 peaks increase gradually with the increasing annealing time, starting from 0 W% for the WO_3_NA sample until reaching 63 W% for the WO_3_A90 sample. A full phase transition into the monoclinic phase does not occur in our samples, as longer times or higher temperatures are needed, as expected.[32] In fact, annealing conditions were chosen to allow a careful modification of hexagonal/monoclinic volume ratio, greatly useful for HER optimization. The size of the h- and m-WO_3 submicrometer crystallites can be calculated by using the Scherrer equation[36] (details are reported in the Supporting Information), which are reported in Figure 2c as a function of the annealing time (error bars are reported for each measurement). It is worth to note that the thermal treatment affects the m-WO_3 crystallite size, which increases with the annealing time. However, h-WO_3 crystallite size does not

https://doi.org/10.1021/acsaem.2c01383
ACS Appl. Energy Mater. 2022, 5, 9702−9710

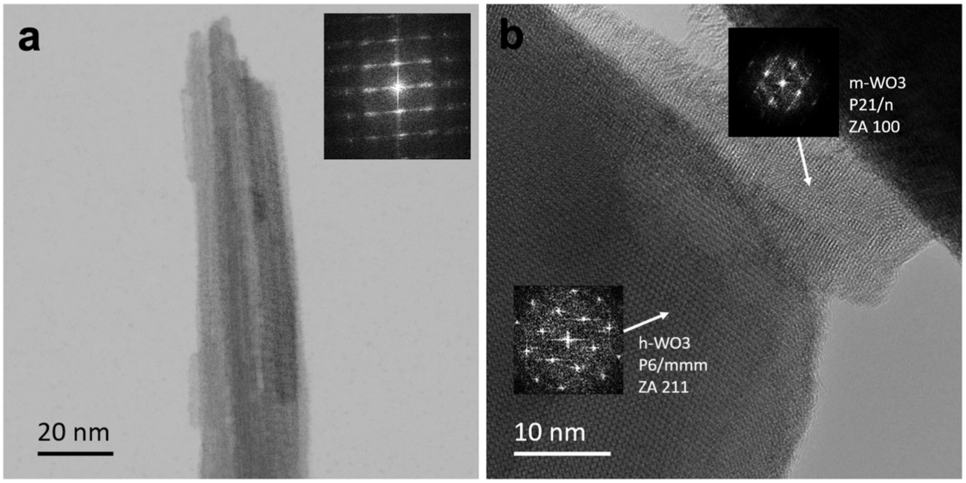

Figure 3. (a) TEM bright-field image of a single nanorod, composed of aligned nanoneedles. (b) High-resolution TEM image which confirms the presence of the h-/m-WO_3 phase junction. Inset: (a) FFT of Figure 3a; (b) FFT of h- and m-WO_3.

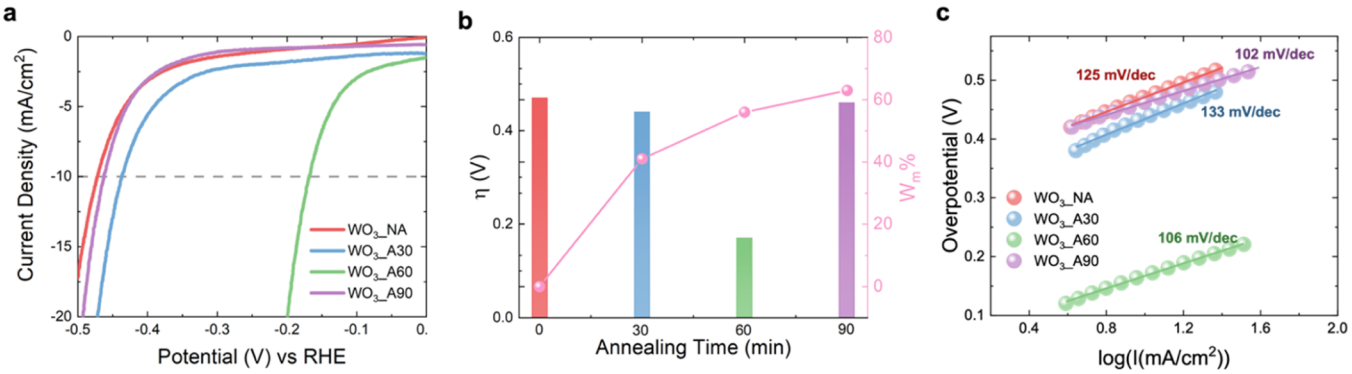

Figure 4. (a) LSV curves, (b) η and W_h% as a function of annealing time, and (c) Tafel plots related to the WO_3_NA (red), WO_3_A30 (blue), WO_3_A60 (green), and WO_3_A90 (violet) electrodes. The dashed line in (a) indicates the current density of 10 mA/cm^2.

depend on the annealing time. The observed reduction of W_h% with annealing suggests a decrease of h-WO_3 crystallite density.

TEM analyses were performed to investigate the morphology and crystal structure of single nanorods. Figure 3a reveals that each nanorod is composed of a bundle of smaller needles (about 10 nm large) probably stuck together during the hydrothermal synthesis. These needles are well-aligned with each other, with the main dimension along the *c*-axis, as shown by the fast Fourier transforms (FFTs) in the inset. Interestingly, the high-resolution micrograph of a WO_3 nanoneedle (Figure 3b) clearly shows a phase junction among the hexagonal and monoclinic structures (confirmed by the respective FFTs in the insets). Such evidence confirms the presence of h-/m-WO_3 phase junctions in the WO_3_A60 powder, as expected from the XRD results.

3.2. Electrochemical Characterization. Figure 4a shows the iR_u-corrected LSV curves reported versus the RHE scale (eqs 1 and 2) of WO_3_NA-, WO_3_A30-, WO_3_A60-, and WO_3_A90-based electrodes, at a scan rate of 5 mV/s. All the polarization curves show a similar trend, with an initial current density plateau, followed by a rapid increasing current density, evidencing a more and more pronounced H_2 production. WO_3_NA and WO_3_A90 electrodes (red and violet curves, respectively) show almost overlapping polarization curves by revealing a similar HER behavior. The WO_3_A30 electrode polarization curve (blue curve) shows a little improvement in terms of current density produced at a fixed potential. The WO_3_A60 electrode (green curve) shows an excellent polarization curve with a strong current density at a moderately low negative potential, revealing a very good electrocatalytic HER activity. In detail, the overpotential at 10 mA/cm^2 (η) of the WO_3_A60 electrode is 170 mV, whereas WO_3_NA, WO_3_A30, and WO_3_A90 electrodes show η values of about 460 mV (η values are listed in Table S1). The supremacy of HER performance of the WO_3_A60 electrode can also be appreciated by its current at an overpotential of 170 mV (10 mA/cm^2), which is 10 times higher than that of WO_3_NA, WO_3_A30, and WO_3_A90 electrodes at the same overpotential. The annealed series from 30 to 90 min was experimentally reproduced two times, confirming the best outcomes for 60 min annealing.

The η and crystal phase mixture trends as a function of the annealing time are reported in Figure 4b. By increasing W_m% up to 56%, η decreases to its minimum value (170 mV for WO_3_A60). A further increase of W_m% (63%) leads to a worsening of the HER catalytic activity, which becomes comparable to that of the fully hexagonal phase. Such a behavior clearly indicates that a mixture of phases is better than a single phase. While it is clearly established that a fully hexagonal phase is much better than a fully monoclinic one,[10,15] here, we demonstrate that when the hexagonal and monoclinic phases coexist at a comparable extent, the highest HER performance is obtained.

https://doi.org/10.1021/acsaem.2c01383
ACS Appl. Energy Mater. 2022, 5, 9702−9710

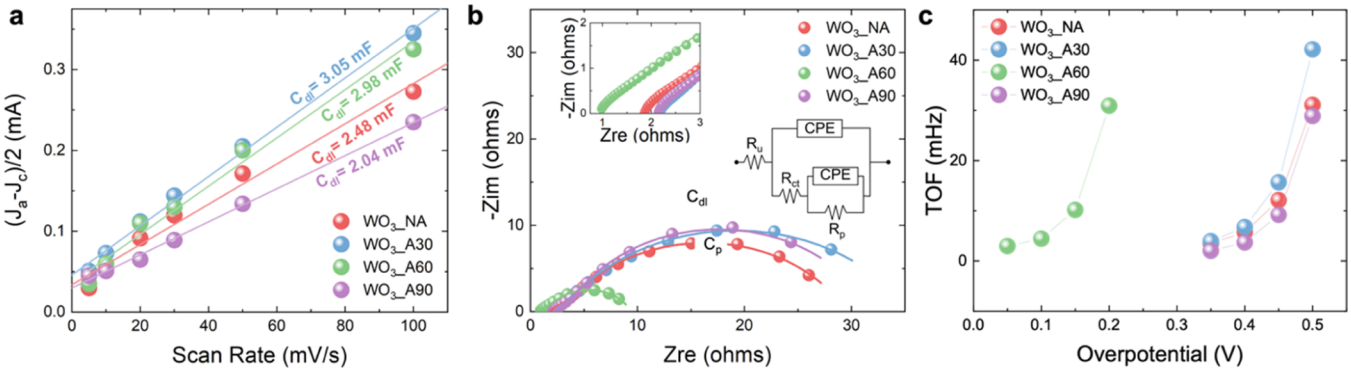

Figure 5. (a) Plot of (J_a−J_c) recorded at −0.25 V vs the scan rate (solid sphere) and related linear fits (solid line). (b) EIS analyses and (c) TOF as a function of the overpotential of WO_3_NA (red), WO_3_A30 (blue), WO_3_A60 (green), and WO_3_A90 (violet) electrodes. Inset: Armstrong and Henderson equivalent circuit and the magnification of the high-frequency region.

To deepen such experimental evidence, we analyzed the kinetics of HER in our samples. Figure 4c shows the Tafel plot and the relative linear fit of WO_3_NA, WO_3_A30, WO_3_A60, and WO_3_A90 electrodes (filled circle curves and solid lines, respectively) obtained from the polarization curves of Figure 4a (details are reported in the Supporting Information). All Tafel plots show the same slope, in the range of 100−130 mV/dec (values are listed in Table S1). A slightly lower Tafel slope seems to be related to a higher monoclinic volume ratio, even if the variation among all samples is fairly limited. The lack of variation in the Tafel slope is an index of the same HER mechanism, regardless of the hexagonal and monoclinic contents in WO_3. The Tafel slope is strictly related to the rate-determining step (RDS) among the elementary characteristic steps through which HER occurs.[37] According to Tian et al., the HER process in an acidic environment occurs through the combinations of the following steps, namely, the Volmer, Tafel, and Heyrovsky equations, respectively:[37]

$$H^+ + e^- + {}^*{=}H_{ads} \tag{3}$$

$$H_{ads} + H_{ads} = H_2 + 2^* \tag{4}$$

$$H_{ad} + H^+ + e^- = H_2 + {}^* \tag{5}$$

where * denotes the active adsorption site. In detail, the HER occurs through a Volmer−Tafel or a Volmer−Heyrovsky mechanism, depending on the electrode material. Moreover, the Tafel slope around 118 mV/dec is typically related to the HER for which the Volmer process acts as the RDS.[37] Such a situation describes all our WO_3-based electrodes, for which the HER process is limited by the H^+ adsorption process on the electrode surface. Such evidence is not in contrast with the variation of the W_h%/W_m% ratio, as this last parameter fairly regards the bulk material, while the H adsorption process occurs at the surface.

The HER activity was further evaluated by calculating the ECSA parameter, as described in the Supporting Information. Figure S1 shows the CV curves recorded in a nonfaradic region, between −0.3 to −0.2 V versus SCE, at different scan rates ranging between 5 and 100 mV/s of (a) WO_3_NA, (b) WO_3_A30, (c) WO_3_A60, and (d) WO_3_A90 electrodes. Figure 5a shows the plot of (J_a−J_c) recorded at −0.25 V from the CV curves of Figure S1 versus the scan rate (red, blue, green, and violet solid spheres) and the related linear fits (red, blue, green, and violet solid lines) which allow defining C_{dl} at −0.25 V.[3] The ECSA parameter is defined (details in the Supporting Information). The C_{dl} and ECSA values are listed in Table S1. The C_{dl} (ECSA) values are comparable for the WO_3 electrodes with an intermediate m-WO_3 content (3.05 mF (102 cm^2) and 2.98 mF (100 cm^2) for WO_3_A30 and WO_3_A60, respectively), while they are slightly lower for the WO_3 electrodes with the prevalence of a hexagonal or monoclinic crystalline phase (2.48 mF (83 cm^2) and 2.04 mF (68 cm^2) for WO_3_NA and WO_3_A90, respectively). The slightly higher C_{dl} and ECSA values for WO_3_A60 are not high enough to explain its excellent catalytic HER activity. Thus, further in-depth electrochemical analyses were carried out.

The charge transfer kinetics occurring at the interface between the electrolyte and the WO_3-coated electrode was investigated by using EIS analysis. Figure 5b shows the Nyquist plot for all the WO_3-based electrodes (solid spheres). All the EIS spectra exhibit a hint of a very small (inset of Figure 5b) and a large semicircle in the higher and lower frequency regions, respectively. The impedance data were interpreted and fitted (solid line in Figure 5b) using the equivalent circuit of Armstrong and Henderson reported in Figure 5b. R_u represents the uncompensated resistance used in eq 2 for the iR_u correction of the LSV current, R_{ct} represents the charge transfer resistance related to the substrate electrode reaction, R_p is related to the mass charge resistance of the intermediate H_{ads} on the surface of the catalytic material which is also called *pseudo-resistance*, and C_{dl} and C_p are constant phase capacitances, which represent the double-layer capacitance and pseudo-capacitance (at η), respectively, and are described by pre-exponential (P_{dl} and P_p) and exponential (n_{dl} and n_p) factors.[38] All fit values are reported in Table 1. P_{dl} and n_{dl} are similar for all WO_3-based electrodes as well as P_p and n_p. The R_{ct} values are similar to each other, regardless of the crystal phase composition of WO_3 nanostructure-based electrodes, confirming that the substrate role is the same as well as the substrate coverage for all WO_3-based electrodes. The sum of R_{ct} and R_p represents the total faradaic resistance of the

Table 1. EIS Parameters of WO_3_NA, WO_3_A30, WO_3_A60, and WO_3_A90 Electrodes

	P_{dl} ($\times10^{-3}$)	n_{dl}	P_p ($\times10^{-3}$)	n_p	R_u (ohm)	R_{ct} (ohm)	R_p (ohm)
WO_3_NA	1	0.7	4	0.7	1.9	2.3	25.4
WO_3_A30	3	0.7	5	0.7	2.2	2.3	31
WO_3_A60	0.4	0.8	5	0.7	2	1.2	7.3
WO_3_A90	1	0.7	2	0.7	2.1	2.7	27

https://doi.org/10.1021/acsaem.2c01383
ACS Appl. Energy Mater. 2022, 5, 9702−9710

Table 2. Comparison between the Electrochemical HER Parameters for WO_3-Based Nanostructures Reported in the Literature and Our Data

	η (mV)	Tafel slope (mV/dec)	C_{dl} (mF)	ECSA (cm^2)	TOF@η (mHz)	ref
WO_{3-x} nanoplates on carbon nanofibers	185	89				11
WO_3@NPRGO	225	87				17
$WO_3 \cdot H_2O$ nanoplates	300	97				39
Ag-WO_3	207	52.4	54.92			40
WS_2−WC−WO_3	312	59	11.8	295	20	28
WS_2/WO_3 heterostructure	395	50				29
h-WO_3/m-WO_3 nanorods	170	106	2.98	100	15	our work

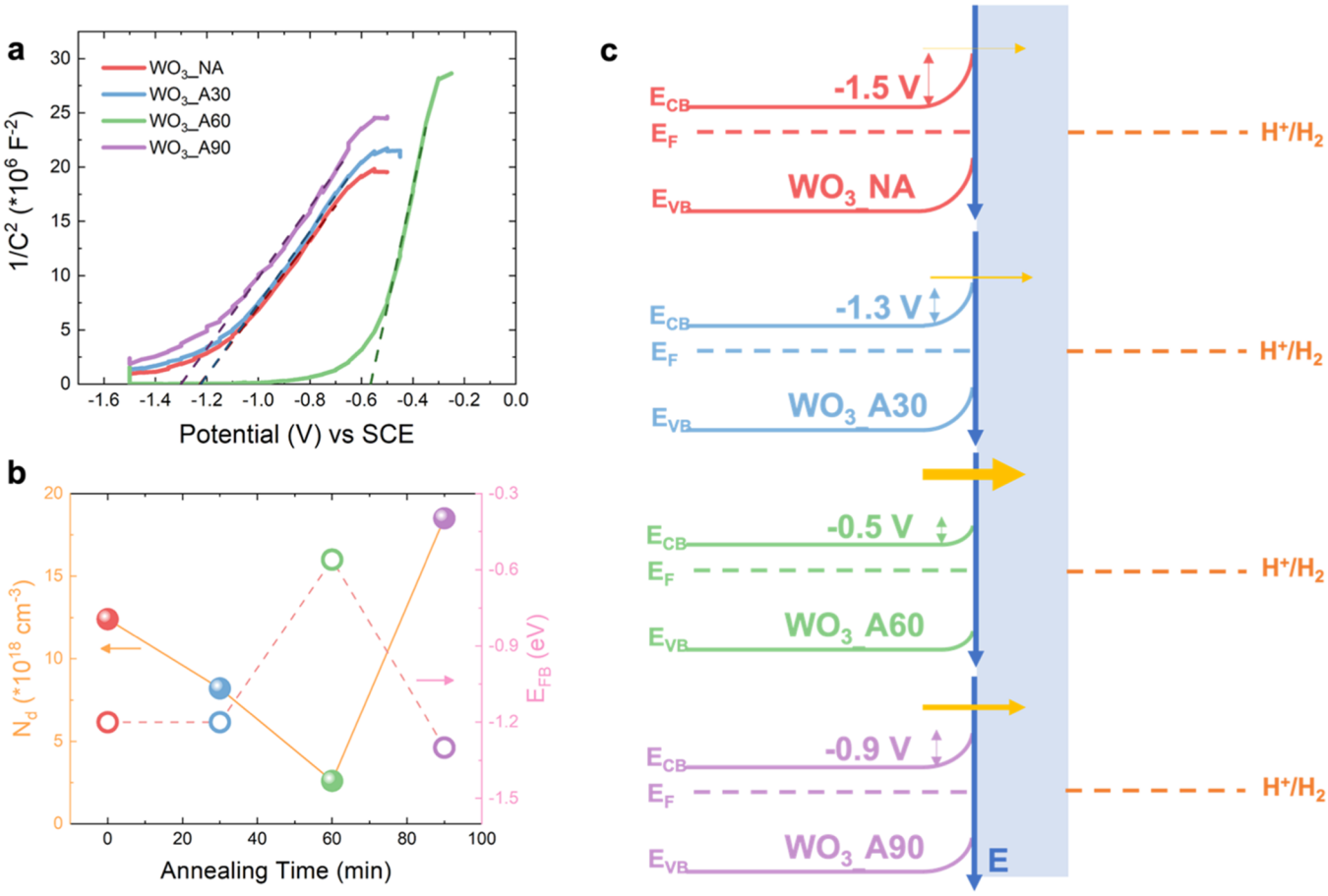

Figure 6. (a) Mott−Schottky plot and (b) related donor concentration (N_d) and flat-band potential (E_{FB}) of WO_3_NA (red), WO_3_A30 (blue), WO_3_A60 (green), and WO_3_A90 (violet) electrodes; (c) scheme of the relative position of energy levels and band bending related to the H^+/H_2 energy level at the semiconductor−liquid interface for each WO_3-based electrode. The thickness of the yellow arrow denotes the magnitude of the cathodic current.

electrode at a fixed potential.[38] The smallest value of R_p, which results into the smallest faradaic resistance, is obtained for the WO_3_A60 electrode which possesses the highest HER activity. As R_{ct} and R_p are strictly correlated to the active Volmer, Tafel, or Heyrovsky mechanisms, the catalytic activity of the WO_3_A60 electrode can be ascribed to a more favorable H^+ adsorption on the surface, thanks to the lowering of the total faradaic resistance of the HER mechanism, by pointing out the correlation between the H^+ adsorption process and the phase junction formation, which depends on the m-WO_3 and h-WO_3 contents in WO_3-based electrodes.

To further study the HER activity of WO_3-based electrodes, the turnover frequency (TOF) is calculated as a function of the overpotential, as described in the Supporting Information and reported in Figure 5c. The TOF of WO_3-based electrodes at η is about the same (the values are listed in Table S1), thus confirming that the only relevant difference in the HER activity between the WO_3-based electrodes is the potential at which the HER starts.

The electrochemical HER parameters of the WO_3_A60 electrode are reported in Table 2 for a comparison with the data reported in the literature for WO_3-based electrodes. Our electrode shows the lower overpotential, confirming the promising HER performances of h-WO_3/m-WO_3 phase junction-based nanostructures. The presence of two crystal phases at comparable extents could be responsible for this advantageous performance.

3.3. Effect of the Phase Junction Formation. To better understand the effect of phase junction formation in the WO_3 HER catalytic activity, Mott−Schottky analysis was carried out,

https://doi.org/10.1021/acsaem.2c01383
ACS Appl. Energy Mater. 2022, 5, 9702−9710

in 1 M H_2SO_4 aqueous solution, for the study of the liquid–semiconductor interface. WO_3-based electrodes were characterized by measuring their capacitance as a function of applied potential.[41−43] The typical Mott–Schottky plot (C^{-2} vs applied potential) is shown in Figure 6a. A linear trend from −1.1 to −0.7 V versus SCE is shown for WO_3_NA, WO_3_A30, and WO_3_A90 electrodes and from −0.5 to −0.4 V for the WO_3_A60 electrode. The flat-band potential E_{FB} and the donor density N_d are calculated as the x-axis intercept and slope from the linear part of the plot, as described in the Supporting Information, and are reported in Figure 6b (filled and hollow spheres, respectively).[41−44] The minimum E_{FB} value (−0.5 V) is obtained for the WO_3_A60 electrode, for which lower N_d (2.6×10^{18} cm^{-3}) is recorded (do note the inverse Y scales for E_{FB} and N_d in Figure 6b). E_{FB} is related to band bending at the liquid–semiconductor interface under equilibrium conditions; so, by combining this value with the open-circuit potential (OCP) of each WO_3-based electrode (reported in Table S2), the actual band bending with respect to the H^+/H_2 level can be defined. The results of such exercise are reported in Figure 6c. The WO_3_A60 electrode shows the lowest band bending as well as the lowest depletion region, which leads to the lowest energy barrier for electrons moving from WO_3 toward the electrolyte (depicted as the light blue region). A larger electron flux is thus expected for this sample (as drawn by the thickness of yellow horizontal arrows) in comparison to others. Lower band bending corresponds to a lower η for HER, explaining the better catalytic activity of the WO_3_A60 electrode.

The evidence can be summarized as follows:

(i) XRD and TEM analyses demonstrate the h-/m-WO_3 phase junction formation. W_m% strongly depends on the annealing time, as well as the monoclinic crystallite size;

(ii) WO_3_NA, WO_3_A30, WO_3_A60, and WO_3_A90 electrodes show polarization curves with the same trend (Figure 4a), but the polarization curve of WO_3_A60 is shifted toward lower potentials by achieving lower η of 170 mV at 10 mA/cm^2;

(iii) The Tafel slopes and TOF values of WO_3-based electrodes suggest that the HER mechanism is the same, regardless of the m-WO_3 and h-WO_3 contents, and so of the phase junction formation. Moreover, the Tafel slope values suggest that the HER mechanism is limited by the H^+ adsorption mechanism on the active material surface;

(iv) WO_3_NA, WO_3_A30, WO_3_A60, and WO_3_A90 electrodes show similar C_{dl} and ECSA by ruling out the active surface role in the HER catalytic activity and in the phase junction formation;

(v) EIS analysis shows the same quasi-negligible electrode substrate role for each WO_3-based electrode and the possibility to ascribe the superior HER activity of the WO_3_A60 electrode to a lowering of the total faradic resistance of the HER mechanism caused by the m-WO_3 and h-WO_3 phase junction formation.

(vi) Mott–Schottky analyses highlight the energy-level structure at the semiconductor–liquid interface, revealing the smallest band bending for the WO_3_A60 electrode, which leads to the highest cathodic current flux toward the electrolyte and so to the lowest η for the activation of the HER process.

Taking into account these considerations, a schematic representation of the correlation between the enhancement of the HER activity and the formation of m- and h-WO_3 phase (lilac and brown parts, respectively) junctions is proposed in Figure 7. The thermal treatment leads to a stable phase junction formation corresponding to the grain boundary between h- and m-WO_3 crystallites (red lines in Figure 7) without affecting the morphology of WO_3-based nanostructures, as shown by the SEM images in Figure 1. As depicted in Figure 7, the concentration of the h-/m-WO_3 phase junctions depends on the annealing time and so on W_h% and W_m%. The WO_3_A60 powder shows similar W_h% and W_m% values (see Figure 2b) and similar h- and m-WO_3 crystallites sizes (see Figure 2c), which should lead to a higher density of phase junctions. On the contrary, the WO_3_NA, WO_3_A30, and WO_3_A90 powders show a lower (or zero) phase junction density because of the prevalence of one crystal phase. At the semiconductor–liquid interface, the phase junctions affect the total band bending (Figure 6c). The lower band bending results in a higher cathodic current and hence in a higher concentration of available electrons useful to lower the total faradaic resistance. The phase junction interface becomes the main site for H^+ adsorption and for H_2 production thanks to the largely available electrons, as shown in Figure 7. The presence of a high concentration of phase junction lowers the required potential for HER activation, and so η, confirming our experimental evidences related to WO_3_A60.

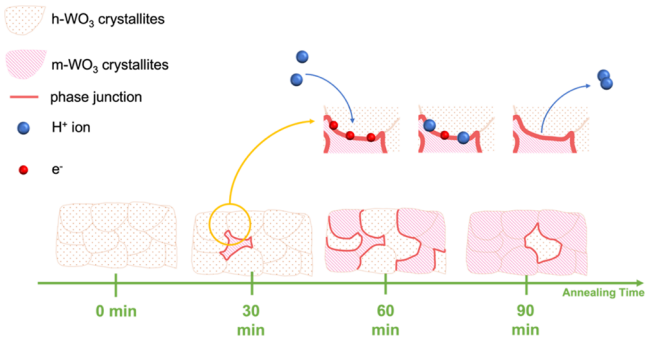

Figure 7. Schematic representation of the HER mechanism corresponding to the h-/m-WO_3 phase junction (brown and pink areas). The HER predominantly occurs at the phase junction interface (red lines), in which many electrons (red balls) are available for the adsorption of H^+ (blue balls) and production of H_2.

4. CONCLUSIONS

In conclusion, h-/m-WO_3 phase junction has been successfully fabricated in the hydrothermally synthesized WO_3 nanorods, annealed at 400 °C for 30, 60, and 90 min. The hexagonal and monoclinic contents strongly depend on the annealing time as well as the dimension of the as-formed monoclinic crystallites. In particular, the 60 min annealed WO_3 powders show a monoclinic content of 56% and comparable monoclinic and hexagonal crystallite sizes. This sample exhibits exceptional catalytic activity for HER in 1 M H_2SO_4 electrolyte with an overpotential of 170 mV at 10 mA/cm^2. The advantage of this h-/m-WO_3 combination can be ascribed to the formation of numerous phase junction interfaces at which the HER can occur faster thanks to the larger availability of electrons, as demonstrated by the Tafel, EIS, and Mott–Schottky analyses and ECSA and TOF determination. The obtained catalyst

https://doi.org/10.1021/acsaem.2c01383
ACS Appl. Energy Mater. 2022, 5, 9702−9710

represents a potential candidate for Pt-free electrochemical production of clean hydrogen in acid solution by paving the way to a further study and engineering of simple phase junction formation in semiconductors for Pt-free HER applications.

■ ASSOCIATED CONTENT

Supporting Information

The Supporting Information is available free of charge at https://pubs.acs.org/doi/10.1021/acsaem.2c01383.

Description of the RIR method and the application of the Scherrer formula; calculation of the Tafel slope, ECSA, and TOF parameters; description of the Mott−Schottky analysi s; h-WO_3 content, η, Tafel slope, C_{dl}, ECSA, and TOF of WO_3_NA, WO_3_A30, WO_3_A60, and WO_3_A90 electrodes; results of Mott−Schottky analyses for WO_3_NA, WO_3_A30, WO_3_A60, and WO_3_A90 electrodes; CV at different scan rates in the non-faradic region ranging between −0.3 and −0.2 V vs SCE of (a) WO_3_NA, (b) WO_3_A30, (c) WO_3_A60, and (d) WO_3_A90 (violet) electrodes (PDF)

■ AUTHOR INFORMATION

Corresponding Author

Salvo Mirabella − *Dipartimento di Fisica e Astronomia "Ettore Majorana", Università degli Studi di Catania, Catania 95123, Italy; CNR-IMM (Catania Università), Catania 95123, Italy;* orcid.org/0000-0002-9559-4862; Email: salvo.mirabella@dfa.unict.it

Authors

Giacometta Mineo − *Dipartimento di Fisica e Astronomia "Ettore Majorana", Università degli Studi di Catania, Catania 95123, Italy; CNR-IMM (Catania Università), Catania 95123, Italy;* orcid.org/0000-0001-6713-8811

Mario Scuderi − *Institute for Microelectronics and Microsystems, National Research Council (CNR-IMM), Catania I-95121, Italy;* orcid.org/0000-0001-9026-5317

Elena Bruno − *Dipartimento di Fisica e Astronomia "Ettore Majorana", Università degli Studi di Catania, Catania 95123, Italy; CNR-IMM (Catania Università), Catania 95123, Italy*

Complete contact information is available at: https://pubs.acs.org/10.1021/acsaem.2c01383

Author Contributions

The manuscript was written through contributions of all authors. All authors have given approval to the final version of the manuscript.

Funding

This work was supported by programma ricerca di Ateneo UNICT 2020−22 linea 2 PIA.CE.RI "NaTI4Smart Sviluppo di NAnomateriali e Tecnologie Innovative per Smart detection", and by PRIN 2017 "CLEAN-Valorizing Sustainable Plastics through a CLEver use of NANoparticles" 20174FSRZS_003.

Notes

The authors declare no competing financial interest.

■ ACKNOWLEDGMENTS

The authors wish to thank G. Malandrino (University of Catania, Italy) for useful discussions and experimental XRD contribution, the Bio-nanotech Research and Innovation Tower (BRIT) laboratory of the University of Catania (Grant no. PONa3_00136 financed by the MIUR) for the Smartlab diffractometer facility, and G. Pantè, C. Percolla, and S. Tatì (CNR-IMM Catania, Italy) for technical support.

■ REFERENCES

(1) Anantharaj, S.; Ede, S. R.; Karthick, K.; Sam Sankar, S.; Sangeetha, K.; Karthik, P. E.; Kundu, S. Precision and Correctness in the Evaluation of Electrocatalytic Water Splitting: Revisiting Activity Parameters with a Critical Assessment. *Energy Environ. Sci.* **2018**, *11*, 744−771.

(2) Li, Y.; Zhai, X.; Liu, Y.; Wei, H.; Ma, J.; Chen, M.; Liu, X.; Zhang, W.; Wang, G.; Ren, F.; Wei, S. WO3-Based Materials as Electrocatalysts for Hydrogen Evolution Reaction. *Front. Mater.* **2020**, *7*, 1−8.

(3) Sekar, S.; Aqueel Ahmed, A. T.; Pawar, S. M.; Lee, Y.; Im, H.; Kim, D. Y.; Lee, S. Enhanced Water Splitting Performance of Biomass Activated Carbon-Anchored WO3 Nanoflakes. *Appl. Surf. Sci.* **2020**, *508*, No. 145127.

(4) Zheng, T.; Sang, W.; He, Z.; Wei, Q.; Chen, B.; Li, H.; Cao, C.; Huang, R.; Yan, X.; Pan, B.; Zhou, S.; Zeng, J. Conductive Tungsten Oxide Nanosheets for Highly Efficient Hydrogen Evolution. *Nano Lett.* **2017**, *17*, 7968−7973.

(5) Hansen, J. N.; Prats, H.; Toudahl, K. K.; Mørch Secher, N.; Chan, K.; Kibsgaard, J.; Chorkendorff, I. Is There Anything Better than Pt for HER? *ACS Energy Lett.* **2021**, *6*, 1175−1180.

(6) Kibsgaard, J.; Chorkendorff, I. Considerations for the Scaling-up of Water Splitting Catalysts. *Nat. Energy* **2019**, *4*, 430−433.

(7) Gong, M.; Wang, D. Y.; Chen, C. C.; Hwang, B. J.; Dai, H. A Mini Review on Nickel-Based Electrocatalysts for Alkaline Hydrogen Evolution Reaction. *Nano Res.* **2016**, *9*, 28−46.

(8) Safizadeh, F.; Ghali, E.; Houlachi, G. Electrocatalysis Developments for Hydrogen Evolution Reaction in Alkaline Solutions - A Review. *Int. J. Hydrogen Energy* **2015**, *40*, 256−274.

(9) Zhao, G.; Rui, K.; Dou, S. X.; Sun, W. Heterostructures for Electrochemical Hydrogen Evolution Reaction: A Review. *Adv. Funct. Mater.* **2018**, *28*, 1−26.

(10) Zhang, X.; Jin, G.; Wang, D.; Chen, Z.; Zhao, M.; Xi, G. Crystallographic Phase and Morphology Dependent Hydrothermal Synthesis of Tungsten Oxide for Robust Hydrogen Evolution Reaction. *J. Alloys Compd.* **2021**, *875*, No. 160054.

(11) Chen, J.; Yu, D.; Liao, W.; Zheng, M.; Xiao, L.; Zhu, H.; Zhang, M.; Du, M.; Yao, J. WO3-x Nanoplates Grown on Carbon Nanofibers for an Efficient Electrocatalytic Hydrogen Evolution Reaction. *ACS Appl. Mater. Interfaces* **2016**, *8*, 18132−18139.

(12) Ham, D. J.; Phuruangrat, A.; Thongtem, S.; Lee, J. S. Hydrothermal Synthesis of Monoclinic WO3 Nanoplates and Nanorods Used as an Electrocatalyst for Hydrogen Evolution Reactions from Water. *Chem. Eng. J.* **2010**, *165*, 365−369.

(13) Mohamed, M. M.; Salama, T. M.; Hegazy, M. A.; Abou Shahba, R. M.; Mohamed, S. H. Synthesis of Hexagonal WO 3 Nanocrystals with Various Morphologies and Their Enhanced Electrocatalytic Activities toward Hydrogen Evolution. *Int. J. Hydrogen Energy* **2019**, *44*, 4724−4736.

(14) Lv, Y.; Chen, Z.; Liu, Y.; Wang, T.; Ming, Z. Oxygen Vacancy Improves the Hydrogen Evolution Reaction Property of WO3−x Nanosheets. *Nano-Struct. Nano-Objects* **2018**, *15*, 114−118.

(15) Rajalakshmi, R.; Rebekah, A.; Viswanathan, C.; Ponpandian, N. Evolution of Intrinsic 1-3D WO_3 Nanostructures: Tailoring Their Phase Structure and Morphology for Robust Hydrogen Evolution Reaction. *Chem. Eng. J.* **2022**, *428*, No. 132013.

(16) Gong, F.; Yao, C.; Kong, H.; Meng, E.; Gong, L.; Zhang, Y.; Li, F. WO3/C Nanoarchitectures Assembled with 1D Nanowires: The Synthesis, Pt Nanoparticles Decoration, and Highly Enhanced Hydrogen Evolution in Neutral Media. *J. Phys. Chem. Solids* **2022**, *163*, No. 110542.

(17) Hu, G.; Li, J.; Liu, P.; Zhu, X.; Li, X.; Ali, R. N.; Xiang, B. Enhanced Electrocatalytic Activity of WO 3 @NPRGO Composite in a Hydrogen Evolution Reaction. *Appl. Surf. Sci.* **2019**, *463*, 275−282.
(18) Bharagav, U.; Reddy, N. R.; Koteswararao, V. N.; Ravi, P.; Pratap, K.; Sathish, M.; Cheralathan, K. K.; Shankar, M. V.; Kumari, M. M. Heterojunction of CdS Nanocapsules-WO3 Nanosheets Composite as a Stable and Efficient Photocatalyst for Hydrogen Evolution. *Energy Fuels* **2020**, *34*, 14598−14610.
(19) Bekarevich, R.; Pihosh, Y.; Tanaka, Y.; Nishikawa, K.; Matsushita, Y.; Hiroto, T.; Ohata, H.; Ohno, T.; Minegishi, T.; Sugiyama, M.; Kitamori, T.; Mitsuishi, K.; Takada, K. Conversion Reaction in the Binder-Free Anode for Fast-Charging Li-Ion Batteries Based on WO3Nanorods. *ACS Appl. Energy Mater.* **2020**, *3*, 6700−6708.
(20) Pugliese, M.; Prontera, C. T.; Polimeno, L.; Lerario, G.; Giannuzzi, R.; Esposito, M.; Carallo, S.; Costa, D.; De Marco, L.; De Giorgi, M.; Gigli, G.; Sanvitto, D.; Maiorano, V. Highly Reflective Periodic Nanostructure Based on Thermal Evaporated Tungsten Oxide and Calcium Fluoride for Advanced Photonic Applications. *ACS Appl. Nano Mater.* **2020**, *3*, 10978−10985.
(21) Chae, S. Y.; Lee, C. S.; Jung, H.; Joo, O. S.; Min, B. K.; Kim, J. H.; Hwang, Y. J. Insight into Charge Separation in WO3/BiVO4 Heterojunction for Solar Water Splitting. *ACS Appl. Mater. Interfaces* **2017**, *9*, 19780−19790.
(22) Mineo, G.; Ruffino, F.; Mirabella, S.; Bruno, E. Investigation of WO3 Electrodeposition Leading to Nanostructured Thin Films. *Nanomaterials* **2020**, *10*, 1−12.
(23) Sharma, L.; Kumar, P.; Halder, A. Phase and Vacancy Modulation in Tungsten Oxide: Electrochemical Hydrogen Evolution. *ChemElectroChem* **2019**, *6*, 3420−3428.
(24) Ooka, H.; Huang, J.; Exner, K. S. The Sabatier Principle in Electrocatalysis: Basics, Limitations, and Extensions. *Front. Energy Res.* **2021**, *9*, 1−20.
(25) Park, J.; Lee, S.; Kim, H. E.; Cho, A.; Kim, S.; Ye, Y.; Han, J. W.; Lee, H.; Jang, J. H.; Lee, J. Investigation of the Support Effect in Atomically Dispersed Pt on WO3−x for Utilization of Pt in the Hydrogen Evolution Reaction. *Angew. Chem., Int. Ed.* **2019**, *58*, 16038−16042.
(26) Xie, C.; Chen, W.; Du, S.; Yan, D.; Zhang, Y.; Chen, J.; Liu, B.; Wang, S. In-Situ Phase Transition of WO3 Boosting Electron and Hydrogen Transfer for Enhancing Hydrogen Evolution on Pt. *Nano Energy* **2020**, *71*, No. 104653.
(27) Lv, Y.; Liu, Y.; Liu, Y.; Chen, Z.; Zhang, M. CoSe2/WSe2/WO3 Hybrid Nanowires on Carbon Cloth for Efficient Hydrogen Evolution Reaction. *J. Alloys Compd.* **2018**, *768*, 889−895.
(28) Van Nguyen, T.; Do, H. H.; Tekalgne, M.; Van Le, Q.; Nguyen, T. P.; Hong, S. H.; Cho, J. H.; Van Dao, D.; Ahn, S. H.; Kim, S. Y. WS2−WC−WO3 Nano-Hollow Spheres as an Efficient and Durable Catalyst for Hydrogen Evolution Reaction. *Nano Converg.* **2021**, *8*, 28.
(29) Shang, X.; Rao, Y.; Lu, S. S.; Dong, B.; Zhang, L. M.; Liu, X. H.; Li, X.; Liu, Y. R.; Chai, Y. M.; Liu, C. G. Novel WS2/WO3 Heterostructured Nanosheets as Efficient Electrocatalyst for Hydrogen Evolution Reaction. *Mater. Chem. Phys.* **2017**, *197*, 123−128.
(30) Lokhande, V.; Lokhande, A.; Namkoong, G.; Kim, J. H.; Ji, T. Charge Storage in WO 3 Polymorphs and Their Application as Supercapacitor Electrode Material. *Results Phys.* **2019**, *12*, 2012−2020.
(31) Zheng, H.; Ou, J. Z.; Strano, M. S.; Kaner, R. B.; Mitchell, A.; Kalantar-Zadeh, K. Nanostructured Tungsten Oxide - Properties, Synthesis, and Applications. *Adv. Funct. Mater.* **2011**, *21*, 2175−2196.
(32) Kang, M.; Liang, J.; Wang, F.; Chen, X.; Lu, Y.; Zhang, J. Structural Design of Hexagonal/Monoclinic WO3 Phase Junction for Photocatalytic Degradation. *Mater. Res. Bull.* **2020**, *121*, No. 110614.
(33) Lu, Y.; Liu, G.; Zhang, J.; Feng, Z.; Li, C.; Li, Z. Fabrication of a Monoclinic/Hexagonal Junction in WO3 and Its Enhanced Photocatalytic Degradation of Rhodamine B. *Cuihua Xuebao/Chin. J. Catal.* **2016**, *37*, 349−358.
(34) Mineo, G.; Moulaee, K.; Neri, G.; Mirabella, S.; Bruno, E. H2 Detection Mechanism in Chemoresistive Sensor Based on Low-Cost Synthesized WO3 Nanorods. *Sens. Actuators, B* **2021**, *348*, No. 130704.
(35) Yang, M.; Li, J.; Ke, G.; Liu, B.; Dong, F.; Yang, L.; He, H.; Zhou, Y. WO3 Homojunction Photoanode: Integrating the Advantages of WO3 Different Facets for Efficient Water Oxidation. *J. Energy Chem.* **2021**, *56*, 37−45.
(36) Lo Nigro, R.; Malandrino, G.; Fragalà, I. L.; Bettinelli, M.; Speghini, A. MOCVD of CeF3 Films on Si(100) Substrates: Synthesis, Characterization and Luminescence Spectroscopy. *J. Mater. Chem.* **2002**, *12*, 2816−2819.
(37) Tian, X.; Zhao, P.; Sheng, W. Hydrogen Evolution and Oxidation: Mechanistic Studies and Material Advances. *Adv. Mater.* **2019**, *31*, No. e1808066.
(38) Krstajić, N.; Popović, M.; Grgur, B.; Vojnović, M.; Šepa, D. On the Kinetics of the Hydrogen Evolution Reaction on Nickel in Alkaline Solution - Part I. The Mechanism. *J. Electroanal. Chem.* **2001**, *512*, 16−26.
(39) Hu, W. H.; Han, G. Q.; Dong, B.; Liu, C. G. Facile Synthesis of Highly Dispersed WO3·H2O and WO3 Nanoplates for Electrocatalytic Hydrogen Evolution. *J. Nanomater.* **2015**, *2015*, No. 346086.
(40) Ma, J.; Ma, Z.; Liu, B.; Wang, S.; Ma, R.; Wang, C. Composition of Ag-WO 3 Core-Shell Nanostructures as Efficient Electrocatalysts for Hydrogen Evolution Reaction. *J. Solid State Chem.* **2019**, *271*, 246−252.
(41) Chen, Z.; Dinh, H. N.; Miller, E. *Photoelectrochemical Water Splitting: Standards, Experimental Methods, and Protocols*, 2013, vol *126*.
(42) Gelderman, K.; Lee, L.; Donne, S. W. Flat-Band Potential of a Semiconductor: Using the Mott-Schottky Equation. *J. Chem. Educ.* **2007**, *84*, 685−688.
(43) Hankin, A.; Bedoya-Lora, F. E.; Alexander, J. C.; Regoutz, A.; Kelsall, G. H. Flat Band Potential Determination: Avoiding the Pitfalls. *J. Mater. Chem. A* **2019**, *7*, 26162−26176.
(44) Bruno, L.; Strano, V.; Scuderi, M.; Franzò, G.; Priolo, F.; Mirabella, S. Localized Energy Band Bending in Zno Nanorods Decorated with Au Nanoparticles. *Nanomaterials* **2021**, *11*, 2718.

https://doi.org/10.1021/acsaem.2c01383
ACS Appl. Energy Mater. 2022, 5, 9702−9710